frontiers | Frontiers in Physics

TYPE Original Research
PUBLISHED 10 September 2024
DOI 10.3389/fphy.2024.1424755

OPEN ACCESS

EDITED BY
Noaz Nissim,
Soreq Nuclear Research Center, Israel

REVIEWED BY
Emmanuel D'Humières,
Université de Bordeaux, France
Philipp Korneev,
National Research Nuclear University MEPhI, Russia

*CORRESPONDENCE
Artem Kim,
kimtem1@gmail.com

RECEIVED 28 April 2024
ACCEPTED 26 August 2024
PUBLISHED 10 September 2024

CITATION
Kim A, Botton M and Zigler A (2024) Bayesian optimization of proton generation in terawatt laser–CH_2 cluster interactions within a plasma channel.
Front. Phys. 12:1424755.
doi: 10.3389/fphy.2024.1424755

Bayesian optimization of proton generation in terawatt laser–CH_2 cluster interactions within a plasma channel

Artem Kim*, Mordechai Botton and Arie Zigler

High Intensity Laser Lab, Racah Institute of Physics, Hebrew University of Jerusalem, Jerusalem, Israel

Improving the energy efficiency in generating high-energy proton or boron ions is crucial for advancing the feasibility of neutronless laser-based proton–boron (p-B^{11}) fusion reactions. The primary objective of this work is to optimize the fusion energy efficiency of a proposed advanced p-B^{11} fusion scheme. In the proposed scheme, an ultrashort laser pulse is guided by a plasma channel filled with carbon–hydrogen (CH_2) clusters. The MeV protons are generated by the Coulomb explosion (CE) of the cluster, which, therefore, interact with surrounding boron to produce alpha particles. To evaluate the fusion energy efficiency under various conditions, 2D particle-in-cell (PIC) simulations are used, supplemented with analytical calculations and estimations. The Bayesian optimization (BO) algorithm is utilized to optimize the key interaction parameters. The BO approach allows us to identify optimal cluster and laser parameters that would have higher fusion energy efficiency.

KEYWORDS

proton–boron fusion, high-intensity laser, laser–plasma acceleration, Coulomb explosion, Bayesian optimization

1 Introduction

The proton–boron (p-B^{11}) fusion reaction is highly desired due to its aneutronic nature, which results in a cleaner energy output than that in D-T fusion. One of the promising directions of the research in this field is the possibility of initiating p-B^{11} fusion reactions with laser-driven accelerated ions around the cross-section peak with the center of mass energy of ions at approximately 650 keV [1, 2]. The development of ultrafast laser technologies has shown that it is possible to efficiently accelerate ions in plasma to MeV energies [3], paving the way for applications in p-B^{11} fusion.

As a result, there has been a growing interest in laser-based p-B^{11} fusion in recent years [4–19]. Two mainstream proton–boron fusion schemes that recently demonstrated high alpha-particle yields are pitcher–catcher and in-target configurations. For example, Guiffrida et al. utilized in-target configuration [20] and demonstrated ~3•10^{10}/sr α-particles with a 0.6 kJ, 0.3 ns laser pulse. The pitcher–catcher configurations [5, 21] have also shown a high yield ~10^9/sr with a laser energy of 1.4 kJ. In these experiments, the main target did not utilize the energy efficiency enhancement that has been shown in laser-driven ion-acceleration experiments with various advanced target designs [22–24]. However, several recent works addressed this problem and proposed advanced fusion schemes and advanced target designs for higher energy efficiency. For example, H. Ruhl and G. Korn numerically investigated boron nanorod (BN) interactions with ultra-intense laser

pulses [25]. [4] used a 600 nm hydrocarbon plasma polymer film on top of the BN target in order to increase the proton concentration. Several advanced schemes that utilize a strong magnetic field or hybrid fusion scheme with ps and ns lasers have been proposed to increase energy efficiency [10, 26]. V. Krainov proposed a theory of fusion in BH microdroplets [27]. However, compared to the field of laser-driven proton acceleration, advancements in target nanoengineering are still emerging. Improved control over target design, including both shape optimization and the ion composition control on μm and nm scales, has led to increased ion flux, higher ion energies, and better control over the ion energy spectrum [22, 23]. These developments are pivotal for improving the fusion energy efficiency of the p-B^{11} reaction and can be adapted to the actively developing laser-driven p-B^{11} fusion.

In the current paper, we propose and analyze the fusion energy efficiency during the interaction of high-intensity laser with nanocluster suspensions in a long plasma channel. The proposed scheme features a high-intensity short-pulse laser propagating in a relatively low-density plasma channel generated by capillary discharge [28, 29]. Structured CH_2 targets (clusters) concurrently flow in the plasma channel produced in a BN capillary. The laser can interact with the targets to produce the accelerated protons. When the energy of the accelerated protons is high enough (of the order of 1 MeV), they, in turn, can collide with background low-density boron ions or solid boron walls of the capillary and interact to produce the alpha particles. As the process of laser interaction is carried out in a plasma channel, the laser pulse is confined, and the interaction can be extended to a significant length (defined by laser depletion), which, in turn, increases the process efficiency.

The described scheme will depend on various parameters, such as the laser intensity, cluster radius and density, and pulse duration. The parameter space of the proposed scheme is wide; hence, a thorough theoretical search is required in order to find the optimal conditions for the proposed fusion scheme. Improvements in the computing hardware allow us to collect data for many possible configurations in computationally intense particle-in-cell (PIC) simulations within a reasonable amount of time. At such rates, the amounts of data that can be extracted are sufficient to apply advanced numerical techniques such as optimization algorithms and machine learning methods to deal more efficiently with multidimensional problems. Recent works applied Bayesian optimization to both PIC simulations to find the optimal simulation parameters and experiments for the real-time optimization of the experiment setup [30–32]. The ability of a deep neural network to model complex physical phenomena in laser–plasma physics was also assessed for the typical laser-driven ion acceleration scheme [33]. The comprehensive overview of the data-driven techniques applied to laser–plasma physics by [34] emphasizes the huge potential of advanced numerical techniques in the enhancement of experimental and simulation approaches. Thus, to optimize the fusion energy efficiency for the proposed scheme, we use the Bayesian optimization (BO) method due to the computationally intense nature of PIC simulations.

In this paper, we describe a method that uses Gaussian process regression [35] within BO to examine the variables involved in the laser-driven Coulomb explosion (CE) of CH_2 clusters inside the plasma channel. We aim to improve the laser ion conversion efficiency, which will result in better fusion energy efficiency by adjusting various influencing parameters. By applying Bayesian optimization, we seek to better understand and adjust the relationships between these parameters, thereby enhancing the output of fusion energy in our proposed model.

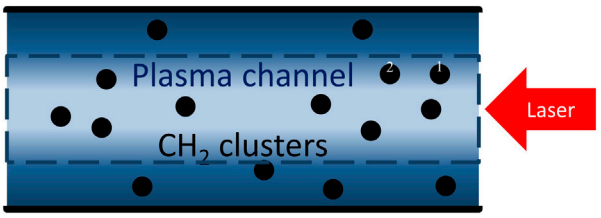

FIGURE 1
Schematic drawing of the p-B^{11} fusion concept (objects not to scale).

2 Materials and methods

2.1 Proton–boron fusion concept

The proposed fusion scheme that has been investigated is shown in Figure 1. In the initial stage, the boron-containing gas is mixed with sub-micron CH_2 clusters as they are injected into the boron-coated capillary. Shortly after the injection, an electrical discharge is used to ionize the gas. The hydrodynamic expansion and cooling of the plasma form a plasma channel that will guide the laser [29, 36]. As the high-intensity pulse propagates through the capillary with the formed channel, it interacts with the clusters, expelling electrons and causing the remaining positively charged cores to undergo a Coulomb explosion. The protons resulting from this explosion are accelerated, and as they propagate, they can interact with the low-density boron plasma and the boron capillary walls. This laser–cluster interaction is crucial for the fusion process as it leads to the production of high-energy protons necessary for p-B^{11} reactions.

According to the proposed fusion scheme, we can calculate the energy of the laser E_L according to Equation 1, which depends on the area of the beam A_{beam}, laser intensity I_0, and full pulse width at half-maximum τ_{FWHM}. We assumed that the laser has a flat-top spatial profile with constant intensity I_0 for the entire area of the plasma channel $A_{channel}=A_{beam}$ and a Gaussian temporal profile. The flat-top profile is required to prevent spatial intensity variation, thus eliminating spatial CE energy dependency for various clusters.

$$E_L(I_0, \tau_{FWHM}) = \int_{-\infty}^{\infty} I_0 \exp\left(-4\ln 2 \frac{t^2}{\tau_{FWHM}^2}\right) dt \propto I_0 A_{beam} \tau_{FWHM}. \quad (1)$$

The total energy released by the fusion reactions E_{tot} from the single-cluster CE is given by Equation 2. It is proportional to the reactivity $\langle \sigma v \rangle$, the energy released in a single fusion reaction E_{fus}, and the number densities of boron n_B and protons n_H and assumes that all reactions occur at a constant rate over time t. The reaction time t, the number density of the solid boron capillary walls n_B, and plasma channel volume V_{ch} are fixed, and the fusion energy released from a single reaction is defined by the reactants.

$$E_{tot} = E_{fus} \langle \sigma v \rangle n_H n_B V_{ch} t = E_{tot}(I_0, \tau, n_0, r). \quad (2)$$

Thus, the fusion energy efficiency G is proportional to the number of protons N_H multiplied by the reactivity $\langle \sigma v \rangle$ and inversely proportional to the laser energy, as shown in Equation 3, and all other values are constant.

$$G = \frac{E_{tot}}{E_L} \propto \frac{N_H \langle \sigma v \rangle}{E_L(I_0, \tau)}. \quad (3)$$

Expanding the reactivity term in (3), we can introduce the single-cluster fusion parameter η_0 Equation 4 that will depend on the ion energy spectrum f(E), the cross-section of the reaction $\sigma(E)$, and the velocity of an ion with energy E v. Unlike the dimensionless fusion energy efficiency G, the single-cluster fusion parameter η_0 does not depend on the boron density and reaction time. This allows us to isolate the laser and cluster parameters for the energy-efficient conversion of the laser into protons, prioritizing energies that match the peaks in the p-B^{11} cross section.

$$\eta_0(n_0, r, I_0, \tau) = \frac{N_H \langle \sigma v \rangle}{E_L(I_0, \tau)} = N_H(r, n_0) \frac{\int_0^{E_{max}} f(E)\sigma(E) v dE}{E_L(I_0, \tau)} \left[cm^3 s^{-1} J^{-1}\right]. \quad (4)$$

The goal of the optimization is to evaluate theoretically and through numerical simulations various cluster densities n_0, cluster radius r, pulse intensity I_0, and pulse duration τ to determine the parameters that will correspond to the higher fusion energy efficiency. The laser propagating through the plasma channel will interact with many clusters, of which many are located in the shadow of other clusters (e.g., cluster 2 is located in the shadow of cluster 1, as shown in Figure 1). Their position along the laser propagation direction is different (*z*-axis), while their position in the *x*–*y* plane is the same, and we have to extend the single-cluster fusion parameter η_0 from Equation 4 to account for all the clusters that would interact with the laser.

In the subsequent paragraph, we analyze the methods used to scale up the calculations of the single-cluster fusion parameter η_0 to encompass the entire volume of the plasma channel with many CH_2 clusters. To analyze the interaction of a laser with a single CH_2 cluster, PIC simulations are employed utilizing numerical code Epoch [37]. The single pre-ionized cluster is positioned in the center of the square 24 μm simulation box with open boundary conditions. The peak of the laser pulse enters the simulation box 50 fs after the start of the simulation. The laser has a Gaussian temporal profile, and the laser waist is much larger than the cluster radius, with a super-Gaussian spatial profile. The grid resolution in the simulation has been adaptively selected based on the radius of the clusters to properly resolve both the cluster and the incident laser wavelength. The carbon ions are assumed to be pre-ionized to C^{2+} and hydrogen to H^+. The plasma is collisionless since even for the lowest electron density that was considered in simulations, the plasma parameter $\Lambda \gg 1$. The Epoch ionization module was not considered to reduce the simulation time.

2.2 Extending the single-cluster fusion parameter η_0 to the plasma channel volume η_{net}

Assuming that the low-density plasma channel does not have a significant effect on the single-cluster interaction, we will not explicitly model the plasma channel in PIC simulations and assume ideal guiding, which is validated by comparative PIC simulations with and without a low-density background plasma channel. To extend the single-cluster results to the volume of the plasma channel, we evaluate the total number of clusters in the cross-section of the plasma channel N_{cross}, as well as η_i,– which is the single-cluster fusion parameters for clusters that face laser intensity I_i affected by the interaction with i−1 clusters. Thus, the net fusion parameter η_{net} that considers all clusters in the volume of the plasma channel can be calculated using N_{cross} and η_i as follows:

$$\eta_{net} = N_{cross}\left(\eta_0(I_0, r, n_0, \tau) + \eta_1(I_1, r, n_0, \tau) + \eta_2(I_2, r, n_0, \tau) + \ldots + \eta_N(I_N, r, n_0, \tau)\right). \quad (5)$$

To extend the single-cluster PIC simulation results to the entire area of the plasma channel, we must calculate the number of clusters in the plasma channel that will interact with the unperturbed intensity. Each cluster, which is characterized by its radius r and density n_0, can be represented by the effective area, which, in turn, is the area of the laser field that was affected by the interaction with the cluster. This effect is shown in Figures 2A, B, which show slices of the 2D intensity profile on a log scale from PIC simulations before and after interaction with r_{clst} = 50 nm and r_{clst} = 800 nm that are located in the center of the simulation box. The horizontal dashed lines illustrate the physical radius of the cluster in each case. Two main effects are discerned. One is intensity reduction, and the other is dispersion of the laser front by the cluster. The 2D intensity maps show that larger radii degrade the laser pulse more significantly, thus restricting the number of successive clusters that can efficiently interact with the same laser pulse.

To avoid extensive PIC simulations, it is necessary to find a suitable model that will describe the area of the laser beam that will be affected by the cluster depending on its size. In this work, the cluster radii are assumed to be in the range $r \in [0.0625, 1]\cdot\lambda_L$ (here, λ_L = 800 nm is the laser wavelength). Accordingly, the Mie solution [38] provides a basic approximation for the effective area S_{eff}. As the PIC simulations in Figure 2 show, for the small cluster, the effective radius is almost the same as the actual cluster radius, while for the larger clusters, the effective radius is significantly larger than the actual radius of the cluster, which aligns with the Mie theory. In Equation 6, the extinction coefficient Q_{ext} is calculated based on the Mie theory and quantifies the total effect of scattering and absorption of light by a spherical particle with radius r relative to its area. The extinction coefficient Q_{ext} was calculated numerically using the *miepython* package.

$$S_{eff} = Q_{ext}\pi r^2; N_{cross} = \frac{A_{beam}}{S_{eff}}. \quad (6)$$

The number of clusters N_{cross} that will interact with unattenuated intensity I_0 can be calculated by dividing the plasma channel area A_{beam} by the effective area of a single cluster S_{eff}.

Next, we need to calculate the effect of η_i from Equation 5 for $i > 0$ from clusters, which are located in the shadows of other clusters inside the plasma channel. We approximated that the laser pulse only loses intensity after interacting with a cluster. The changes in the wavefront, effects of the scattered and reflected light on other clusters, are encompassed by a single intensity reduction parameter.

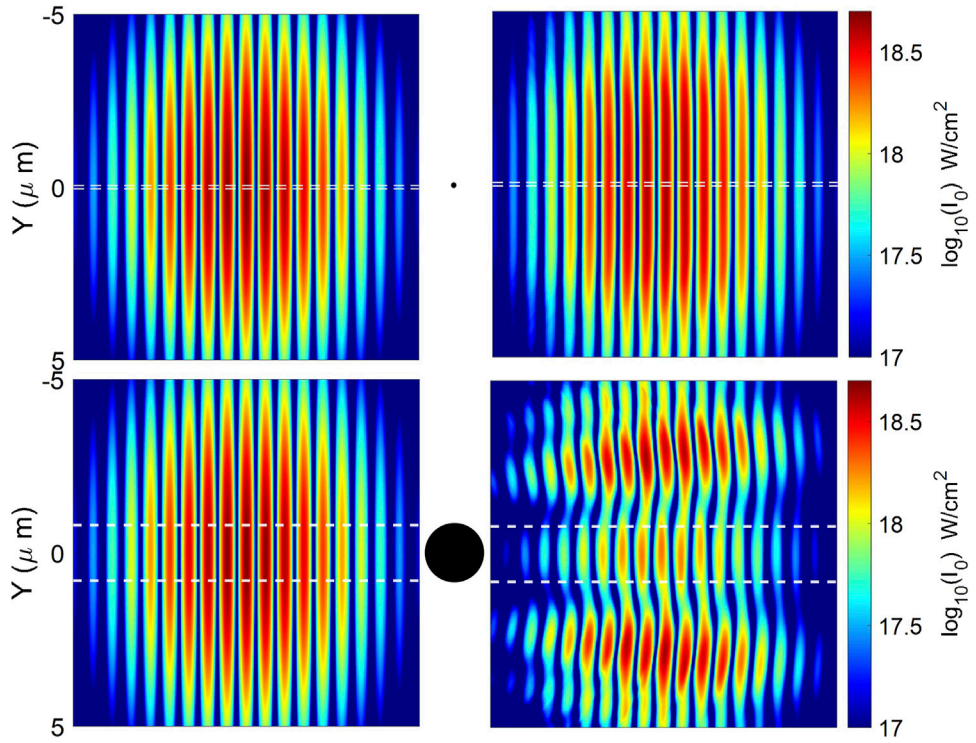

FIGURE 2
Intensity map from 2D PIC simulation before (left) and after (right) the interaction with the clusters with r = 50 nm (top) and r = 800 nm (bottom). The black circles illustrate the position of the cluster. Horizontal dashed lines indicate the radius of the cluster.

TABLE 1 Parameter space used in BO.

Parameter	Value range	Units
Cluster radius, r	[50, 1,000]	nm
Cluster density, n_0 n_{crit}=1.74·10^{21} cm^{-3}	[10, 100]·n_{crit}	cm^{-3}
Laser intensity, I_0	[5, 500]·10^{17}	W/cm^2
Pulse duration, τ	[30, 90]	fs

Under such assumptions, the interaction of a laser pulse with a cluster leads to intensity attenuation due to the absorption and scattering of radiation. A fraction of the laser intensity $I_1 = \alpha I_0$, where $\alpha(r, n_0)$ is the attenuation coefficient, will be transmitted downstream the channel. This attenuation has significant implications for the subsequent clusters. As the laser intensity decreases, the expelled electron charge from each cluster is reduced, reducing the cutoff energy of the accelerated protons. Consequently, this reduction in cutoff energy decreases the number of protons with energies within our region of interest, directly impacting the net fusion parameter η_{net}. We considered various cluster densities and radii, as shown in Table 1. In all cases, the intensity attenuation resulting from the interaction with clusters of various radii can be well approximated by the Beer–Lambert law with a coefficient defined by the PIC simulation results, as shown in Figure 3 for various cluster radii, while density variation had a minor effect on the intensity attenuation coefficient α. The decay coefficient is $\alpha(r) = Ae^{-\mu\frac{r}{\lambda}}$, $A = 0.989 \pm 0.021$, and $\mu = 0.988 \pm 0.075$. For each radius pair, PIC simulations with and without a cluster using various laser intensities [10^{18}, 5•10^{18}, and 10^{19}] W/cm^2 and cluster densities [10, 40, 70, and 100]n_{crit} were performed. The intensity profile that interacted with the cluster was compared to the intensity profile that propagated through the vacuum. The attenuation coefficient was calculated by comparing the longitudinal intensity profile after the interaction with and without a cluster.

The PIC simulations with a fixed target (r=50 nm and n_0=100•n_{crit}) and various intensities showed that proton energy cutoff E_{max} follows the power law scaling as a function of intensity, as shown in Figure 4A. The power law coefficient β is calculated from the 2D Epoch simulations for a given laser intensity I_0 and was used to predict the cutoff proton energy for other intensity values $\beta(r, n_0, I_0\tau) = \frac{E_{cutoff}(r,n_0,I_0,\tau)}{I_0^{\gamma}}$, where γ was calculated from simulations with a fixed target and various intensities $\gamma \approx 0.585$. The Epoch proton energy spectrum shows a complex structure with multiple components. In the low-energy region, the behavior of the distribution function is caused by the slowly expanding core of the cluster, which translates into the CE-accelerated energetic protons that reach a peak and then decay toward the cutoff. The deviation from the ideal square root of energy scaling is caused by the partial removal of electrons from the cluster within our intensity range, which results in a remaining quasi-neutral, slowly exploding core of the cluster, while only the outer layers of the cluster are accelerated to high energies through CE and overestimation of the proton energy cutoff in 2D PIC simulations, compared to the 3D PIC simulations. The normalized proton energy spectrum can be reconstructed using the theoretical model developed by [39]

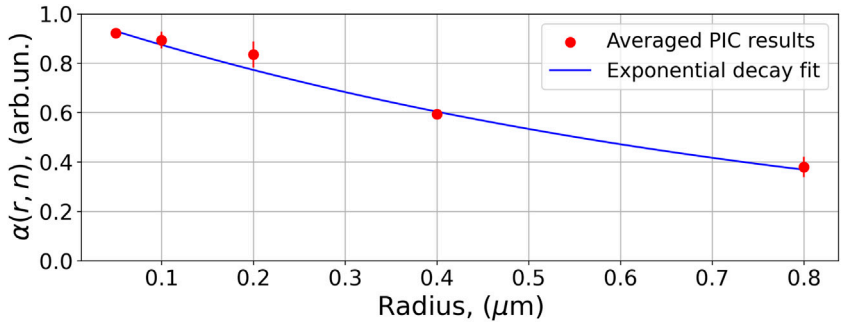

FIGURE 3
Intensity attenuation coefficient α as a function of the cluster radius.

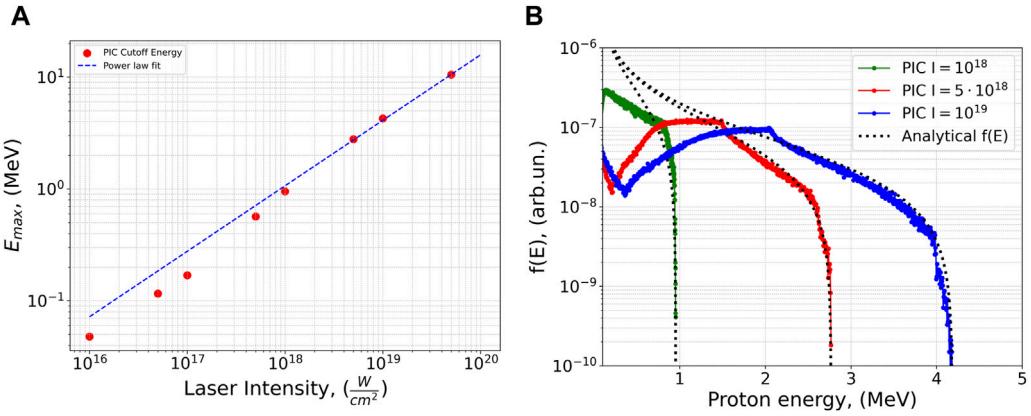

FIGURE 4
(A) PIC cutoff energies and power law fit for a cluster with r = 50 nm and $n_0 = 100\ n_{crit}$. **(B)** Normalized PIC proton energy spectrum for various laser intensities I and analytical probability density function (PDF) based on equations derived by [39].

multiplied by $\xi \approx 3$, which results in a better fit for the high-energy tail of the spectrum, which is our region of interest. An analytical spectrum allows us to extend the single PIC simulation result to interactions with multiple clusters. The subsequent clusters located downward the channel will have a lower cutoff energy due to the intensity attenuation. The cutoff energy of those clusters can be calculated according to the power law scaling of proton cutoff energy. The reconstructed normalized proton energy spectra are shown in Figure 4B, along with the energy spectra obtained from the PIC simulations at times corresponding to the highest proton energy cutoff in the simulation box (typically, at t=710 fs, while t=0 fs corresponds to the interaction of the peak of the pulse with the cluster).

Reconstructed energy spectrums f(E), in turn, are used to calculate the single-cluster fusion parameter η_0 introduced in Equation 4 with the cross-section data for protons with energies in a broad range $E \in [0.05, 9.76]$ MeV based on the analytical approximation presented by [40]. Thus, we can calculate the contribution for each "row" of clusters from layers 1 to N inside the plasma channel, eventually calculating the net fusion parameter η_{net} (7). Clusters in the ith "row" are concealed by the i−1 clusters located closer to the laser pulse in the plasma channel.

$$\eta_{net} = \sum_{i=1}^{N} \eta_i N_{cross} = \sum_{i=1}^{N} N_{cross} \cdot \frac{\int_0^{E_{max(i)}} f_i(E)\sigma(E)v(E)dE}{E_L(I_0, \tau)}. \quad (7)$$

Here, η_i is the fusion parameter of a single cluster interacting with intensity I_i, and N_{cross} is the number of clusters in the cross-section of the plasma channel. The final row N can be evaluated by the attenuated intensity I_n, which becomes too low to produce protons with sufficient energy for fusion reactions.

2.3 Bayesian optimization

Bayesian optimization is a method well suited for optimization problems that are characterized by computationally intensive calculations, such as PIC simulations [41]. It is used to optimize the black-box objective function, such as the net fusion parameter η_{net} described in Equation 7. Thus, η_{net} was chosen as the objective function (a function that is minimized in the optimization process). The BO method uses a surrogate model to estimate the objective function. This model plays a dual role: it attempts to predict the objective function's output and quantifies the uncertainty associated with those predictions, thus allowing us to assess the parameter space and sample the next points from it. For the given parameter

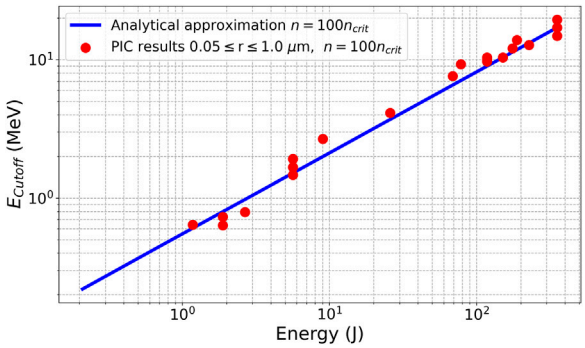

FIGURE 5
Various proton energy cutoffs from PIC simulations and analytical approximation cutoff energy dependency on the laser energy.

space, a Gaussian process regression model is used as a standard surrogate model best suited for low-dimensional (n=4) optimization problems [42]. The expected improvement (EI) acquisition function is chosen due to its good balance between exploration and exploitation [43], ensuring a systematic optimization approach.

The parameter space that needs to be optimized includes the cluster radius r, density n_0, laser intensity I_0, and pulse duration τ and is shown in Table 1. The laser intensity I_0 range was chosen based on the reasonable range of proton energies that can contribute to the p-B^{11} fusion reaction. The cross-section rapidly decreases for protons with energies above 9 MeV and below 150 keV. The pulse duration was added to control the total laser energy while keeping the intensity I_0 the same and maintaining the ultrafast character of the interaction, which has a major impact on the CE process.

The optimization process is orchestrated by a master script, which serves as the primary controlling entity coordinating the entire optimization workflow. The master script connects to the high-performance computing (HPC) cluster and selects initial parameters for the optimization. It generates the necessary input files and submits the simulations to the HPC workload manager, monitoring their progress until completion. Post-processing scripts, initiated by the master script, process the output data from the PIC simulations. As a result, the net fusion parameter η_{net} is used to update the surrogate model. The EI acquisition function determines the next point to sample from the search space. The process iterates, with the updated surrogated model generating new points to evaluate until convergence criteria are met.

3 Results

The optimization results show that an increase in the single-cluster number density n_0 leads to an enhancement of the net fusion parameter η_{net}. This is clear from Equation 7, where an increase in the cluster number density will result in an increase in the proton cutoff energy through enhanced Coulomb explosion and will not affect the laser energy attenuation. If other parameters are fixed, the cluster with higher density would produce more energetic protons and, therefore, will have higher η_{net} due to the CE energy spectrum that is proportional to the square root of energy $\frac{dN}{dE} = C_1\sqrt{E}\cdot H(E_{max} - E)$ [44, 45]. Therefore, we analyze the BO results with the highest density from the parameter space $n = 100n_{crit}$. The proton energy as a function of laser energy for different cluster radii is shown in Figure 5. The analytical approximation of proton cutoff energy for dense clusters shows a reasonable fit with the PIC simulation cutoff energies.

Figures 6A, B show the evolution of various net fusion parameters η_{net} and intensity attenuation during propagation inside the plasma channel under different initial conditions. The *x*-axis shows a dimensionless distance into the plasma channel normalized to the average inter-cluster distance. As we propagate deeper into the plasma channel, we consider interactions with more clusters, and the net fusion parameter increases, while the laser energy decreases due to the interaction with the clusters. The saturation plateau in the fusion parameter is reached in all cases and indicates that a significant part of the laser energy has been lost, and the remaining energy is not sufficient to produce a strong CE of the clusters. In the case of a large radius, the plateau is reached within few iterations, while a small cluster requires several tens of iterations depending on the radius until reaching a plateau. The moderate intensities in the range $5{\cdot}10^{17}$–10^{18} W/cm^2 (red and black lines in Figure 6), regardless of cluster parameters, have higher η_{net} than the high laser intensities (blue and green lines).

This result confirms the existence of optimal energy for a given radius, where η_{net} might be several orders of magnitude larger than in the high-laser energy case. Therefore, for given cluster parameters, η_{net} is expected to exhibit a maximum at a certain moderate laser energy. This will be the optimal laser energy for a given cluster.

To verify the existence of an optimum laser energy for a given cluster and efficiently visualize the 4D parameter space, we consider the laser energy as a single parameter representing the laser intensity and pulse duration, while cluster parameters are categorized into four separate groups depending on the density and radius, as shown in Table 2, which will allow us to identify the edge points for the cluster parameter space:

Splitting the various cluster parameters into different types will allow us to visualize the effect of all parameters on the net fusion parameter η_{net}, which is shown in Figure 7. The small and large high-density clusters η_{net} lie well above all other results and show an efficiency peak at a laser energy close to 2–6 J, while the clusters with low density, regardless of their radius, typically have the lowest fusion parameter η_{net}, as expected from (7), while most of the cases that fall in between the cluster types given in Table 2 lie within the dashed lines connecting the highest and lowest η_{net}. Each of the types indicates the existence of a subtle peak within the laser energy range $2\,J < E_L < 6\,J$, which corresponds to laser intensities $4.2{\bullet}10^{17}$ W/cm^2 and $1.3{\bullet}10^{18}$ W/cm^2 for τ_{FWHM}=60 fs. Since the proton energy cutoff becomes significantly smaller than the required center-of-mass energy for a high-fusion cross-section at very low laser energies $E_L \ll 1$ J, η_{net} should asymptotically approach zero.

Thus, the highest energy efficiency requires a high-density cluster interacting with moderate laser energies. This provides the general direction for the parameter space to reach high energy efficiency. These results were obtained by analyzing all BO outputs. In addition to that, the BO algorithm identified the optimal combination of radius and laser energy within the given parameter space that will lead to the highest energy efficiency.

The following parameters provided the best results: radius r = 50 nm, density n = 100 n_{crit} cm^{-3}, $I_0 = 5\cdot10^{17}$ W/cm^2, and τ=56 fs, leading to $\eta_{net} \approx 2.0\cdot10^{-3}\ cm^3 s^{-1} J^{-1}$. For comparison, the average η in the simulations was $\langle\eta_{net}\rangle \approx 3.3\cdot10^{-4}\ cm^3 s^{-1} J^{-1}$, with $\sigma \approx 4.8\cdot10^{-4}$ resulting in an approximately one order of magnitude increase in the fusion parameter.

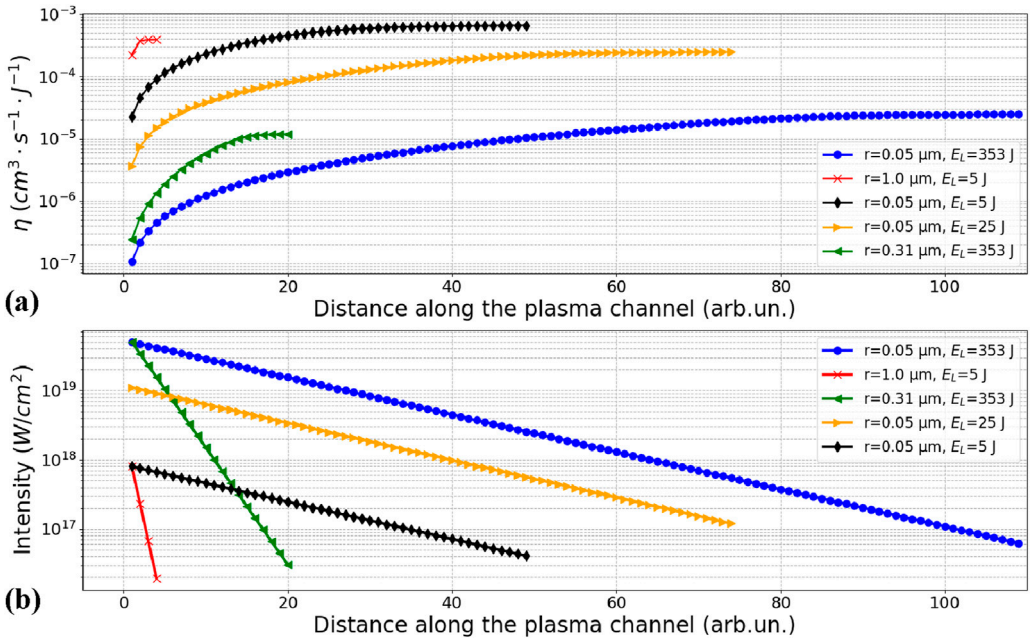

FIGURE 6
(A) Evolution of the net fusion parameter after the interaction with the Nth "row" of clusters according to Equation 5. **(B)** Decay of laser intensity attenuated by the interaction with N clusters.

TABLE 2 Four categories for clusters.

	Cluster radius (nm)	Cluster density (n_{crit})
Small high-density clusters	r < 200	$n_0 > 80 \cdot n_{crit}$
Large high-density clusters	r > 800	$n_0 > 80 \cdot n_{crit}$
Small low-density clusters	r < 200	$n_0 < 20 \cdot n_{crit}$
Large low-density clusters	r > 800	$n_0 < 20 \cdot n_{crit}$

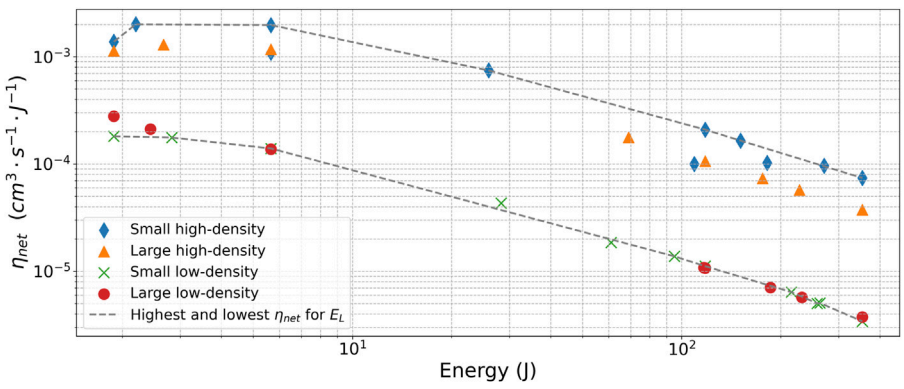

FIGURE 7
Fusion parameter for four cluster types as a function of laser energy.

The convergence plot that illustrates the average and best η_{net} evolution as a function of BO iteration is shown in Figure 8. Each Bayesian optimization iteration consists of four independent PIC simulations with different laser and plasma parameters. The net fusion parameter η_{net} was calculated based on the results of PIC simulations, and the results were used to update the surrogate

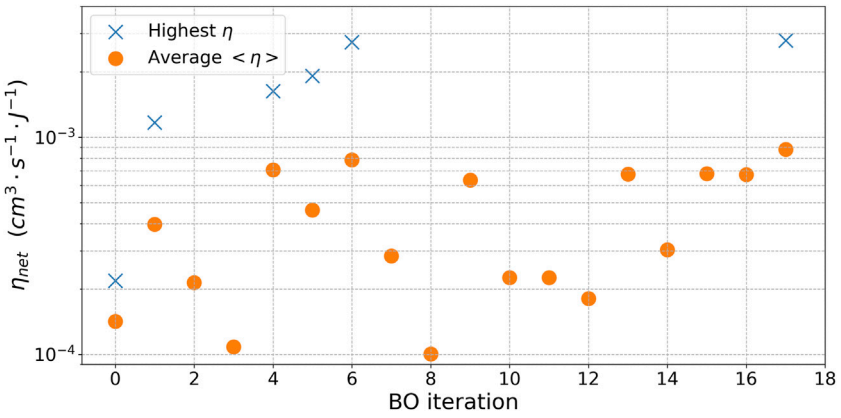

FIGURE 8
Fusion parameter η_{net} as a function of the BO iteration for all simulations.

model. The EI acquisition function samples the next four points from the parameter space to evaluate η_{net}, based on accumulated knowledge. The boundary values for each parameter can vary by few orders of magnitude. This variability provides a broad operational range for parameters such as intensity and radius to identify the optimum. Therefore, even after identifying promising values, the EI continues to explore untested parameters before returning to the best conditions that result in a gradual increase in the average η_{net}.

The smallest radius from the BO parameter space (Table 1) $r = 50\,nm$, which provided the highest net fusion parameter, was limited numerically by the adaptive simulation box size, requiring high resolution for the cluster while maintaining a relatively large box size for the analysis of CE. After identifying optimal density $n = 100n_{crit}$ and energy parameters, we can explore the small radius cases $r < 50\,nm$, estimating the proton energy cutoffs assuming that all electrons are expelled using analytical equations from [45] and use those values to compare the analytical η_{net} with the PIC results that consider that only a fraction of the electrons will be expelled from the cluster, which is shown in Figure 9. The theoretically calculated η_{net} reaches its peak value at r = 2 nm and corresponding blow-off intensity $2{\bullet}10^{16}$ W/cm^2 and decays at higher radiuses due to the rapidly increasing laser intensity, which is required to obtain a full blow-off of electrons, as well as higher proton energies that do not correspond to the peaks in the p-B^{11} cross-section. High-density clusters interacting with moderate laser intensities, where only a fraction of electrons has been expelled, exhibit larger energy efficiency. Among them, the small clusters, with r = 50 nm, had the highest η_{net}. Considering the natural variation in real cluster sizes, we can conclude that in future experiments with the proposed fusion scheme, the optimal cluster size should be smaller, with $2\,nm < r_{best} \leq 50nm$, where a single cluster cannot significantly deteriorate the laser intensity, as shown in Figure 2, which greatly extends the interaction length.

4 Discussion

We introduced a method for optimizing p-B^{11} fusion during the interaction of high-intensity lasers confined inside the plasma channel with clusters. The interaction is optimized so that cluster CE results in a generation of MeV protons and presents several key advantages. Based on our previous experimental works, which demonstrated laser guiding through the plasma channel over long distances, we can effectively increase the interaction length in the proposed scheme. Other advantages demonstrated in this paper include the use of a nanocluster CE approach that leads to the efficient conversion of laser energy to high-energy protons. In addition to that, the CE-based scheme yields a more favorable energy spectrum than the conventional thin-foil targets [46].

Through 2D PIC simulations guided by the BO algorithm, we optimized key interaction parameters such as laser energy and cluster radius and density. The optimization not only aids in identifying optimal conditions for high fusion energy efficiency but also allows us to explore the parameter space and draw conclusions on each of the parameters that can affect the result. Our findings show that high-density clusters, given in Table 2, have higher energy efficiency than low-density clusters due to the increase in the expelled electrons without adversely affecting the laser energy. The cluster radius has an optimum value, which lies between r = 2 nm and r = 50 nm. Additionally, for any given cluster radius and number density within the parameter space, maintaining a moderate laser intensity $I_0 \approx 5 \cdot 10^{17}$ W/cm^2 is crucial for achieving the highest energy efficiency. We can compare the laser to proton energy conversion efficiency in the proposed scheme with other experimental and theoretical results:

BO is particularly suited for complex, computationally demanding problems such as laser–plasma PIC simulations. The probabilistic approach of BO allows it to systematically sample the parameter space, reducing the risk of becoming trapped in a local minimum of the black-box function. The method is well adaptable to unknown, non-linear relationships between input parameters and the output, which are typical for complex laser–plasma interaction problems. This adaptability is crucial for accurately identifying the optimal conditions. The model in BO is continuously updated with each new data point, refining predictions. This feature is particularly beneficial for future experiments with the proposed fusion scheme, where results are received after each laser pulse.

In the future, there will be a need to develop more complex optimization models to account for realistic experiment factors, such as the real spatial profile of the beam, finite precision of the focal-spot position, local density perturbations in the plasma channel, and cluster size distribution. Another limitation of the 2D PIC simulations is the

	Our results (PIC + analytical)	[47] (PIC)	Typical TNSA efficiency [48] (experiments)	[49] (experiment)	[47] (experiment)
Energy range	0.1–1.0 MeV	E_p > 5 MeV	Typically, E_p > 1 MeV	5–30 MeV	0.1–1 MeV
Proton energy in the energy range/laser energy	30%	25%	10%	15%	5%

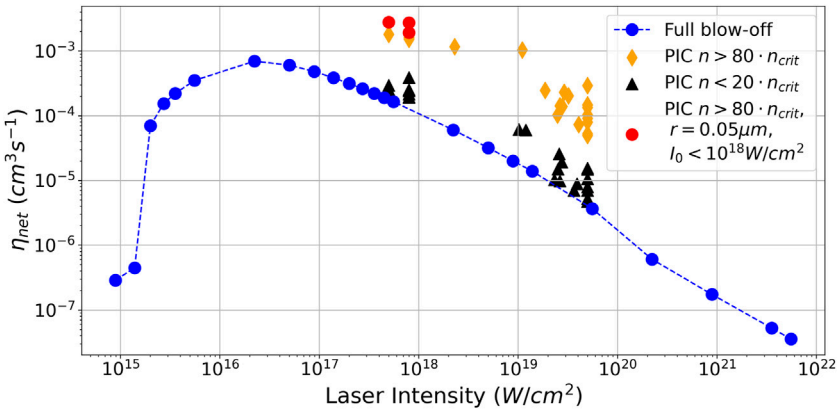

FIGURE 9
BO optimization η_{net} for dense clusters and theoretically calculated η based on the equations derived by [45].

overestimation of the proton energies in cluster Coulomb explosions due to the logarithmic divergence of the accelerating potential in 2D. Therefore, it would be beneficial to perform a series of 3D PIC simulations to obtain a more accurate representation of the energy spectrum and cutoff energies. Despite that, current results serve as a solid starting point for future experiments with the proposed scheme. Additionally, the results presented demonstrate the pivotal role of advanced computational techniques, such as BO, in investigating and optimizing the p-B^{11} fusion energy efficiency. Increasing the fusion energy gain remains an essential problem for advancing fusion as a sustainable energy source. Many p-B^{11} schemes that are currently investigated can benefit from these numerical optimization methods. It is well known that such methods tend to excel with large amounts of data. Thus, it is necessary to develop and integrate such tools into conventional PIC simulations and experiments. This will help accumulate data and accelerate research in the field of laser-based p-B^{11} fusion.

Data availability statement

The raw data supporting the conclusion of this article will be made available by the authors, without undue reservation.

Author contributions

AK: writing–original draft, conceptualization, data curation, formal analysis, investigation, methodology, software, and visualization. MB: writing–review and editing, conceptualization, methodology, project administration, supervision, and validation. AZ: writing–review and editing, conceptualization, funding acquisition, methodology, project administration, resources, supervision, and validation.

Funding

The author(s) declare that no financial support was received for the research, authorship, and/or publication of this article.

Acknowledgments

This work was partially supported by the Israel Ministry of Energy and the Center for Fusion Studies. The authors sincerely appreciate their support.

Conflict of interest

The authors declare that the research was conducted in the absence of any commercial or financial relationships that could be construed as a potential conflict of interest.

Publisher's note

References

1. Tosca M, Molloy D, McNamee A, Pleskunov P, Protsak M, Biliak K, et al. Plasma polymers as targets for laser-driven proton-boron fusion. *Front Phys* (2023) 11. doi:10.3389/fphy.2023.1227140

2. Last I, Ron S, Jortner J. Aneutronic H+B11 nuclear fusion driven by Coulomb explosion of hydrogen nanodroplets. *Phys Rev A* (2011) 83:043202. doi:10.1103/PhysRevA.83.043202

3. Daido H, Nishiuchi M, Pirozhkov AS. Review of laser-driven ion sources and their applications. *Rep Prog Phys* (2012) 75:056401. doi:10.1088/0034-4885/75/5/056401

4. Istokskaia V, Tosca M, Giuffrida L, Psikal J, Grepl F, Kantarelou V, et al. A multi-MeV alpha particle source via proton-boron fusion driven by a 10-GW tabletop laser. *Commun Phys* (2023) 6(6):27–8. doi:10.1038/s42005-023-01135-x

5. Bonvalet J, Nicolaï P, Raffestin D, D'Humieres E, Batani D, Tikhonchuk V, et al. Energetic α -particle sources produced through proton-boron reactions by high-energy high-intensity laser beams. *Phys Rev E* (2021) 103:053202. doi:10.1103/PHYSREVE.103.053202

6. Liu AD, Liu ZY, Li K, Yao YL, Zhou CT, Zhu SP, et al. Enhancement of proton-boron nuclear reactions by utilizing a meshed catcher target. *Phys Rev Appl* (2023) 20:034053. doi:10.1103/PHYSREVAPPLIED.20.034053

7. Daido H, Nishiuchi M, Pirozhkov - AS, Jang S, Kwon R-Y, Linker JA, et al. Perspectives on research on laser driven proton-boron fusion and applications. *J Instrumentation* (2023) 18:C09012. doi:10.1088/1748-0221/18/09/C09012

8. Turcu ICE, Margarone D, Giuffrida L, Picciotto A, Spindloe C, Robinson APL, et al. Borane (B m H n), Hydrogen rich, Proton Boron fusion fuel materials for high yield laser-driven Alpha sources. *J Instrumentation* (2024) 19:C03065. doi:10.1088/1748-0221/19/03/C03065

9. Gruenwald J, Teodorescu C. Novel target design for a laser-driven aneutronic fusion reactor. *Fusion Eng Des* (2020) 151:111397. doi:10.1016/J.FUSENGDES.2019.111397

10. McKenzie W, Batani D, Mehlhorn TA, Margarone D, Belloni F, Campbell EM, et al. HB11—understanding hydrogen-boron fusion as a new clean energy source. *J Fusion Energy* (2023) 42:17–0. doi:10.1007/s10894-023-00349-9

11. Kong D, Xu S, Shou Y, Gao Y, Mei Z, Pan Z, et al. Alpha-particle generation from H-11B fusion initiated by laser-accelerated boron ions. *Laser Part Beams* (2022) 2022:e7. doi:10.1155/2022/5733475

12. Ribeyre X, Capdessus R, Wheeler J, d'Humières E, Mourou G. Multiscale study of high energy attosecond pulse interaction with matter and application to proton–Boron fusion. *Scientific Rep* (2022) 12:4665–14. doi:10.1038/s41598-022-08433-4

13. Azizi N, Hora H, Miley GH, Malekynia B, Ghoranneviss M, He X. Threshold for laser driven block ignition for fusion energy from hydrogen boron-11. *Laser Part Beams* (2009) 27:201–6. doi:10.1017/S0263034609000263

14. Ochs IE, Fisch NJ. Lowering the reactor breakeven requirements for proton-boron 11 fusion. *Phys Plasmas* (2024) 31:12503. doi:10.1063/5.0184945

15. Scholz M, Król K, Kulińska A, Karpiński L, Wójcik-Gargula A, Fitta M. On the possibility of initiating the proton–boron nuclear fusion reaction in the plasma-focus device. *J Fusion Energy* (2019) 38:522–30. doi:10.1007/s10894-019-00225-5

16. Baccou C, Depierreux S, Yahia V, Neuville C, Goyon C, De Angelis R, et al. New scheme to produce aneutronic fusion reactions by laser-accelerated ions. *Laser Part Beams* (2015) 33:117–22. doi:10.1017/S0263034615000178

17. Labaune C, Baccou C, Yahia V, Neuville C, Rafelski J. Laser-initiated primary and secondary nuclear reactions in Boron-Nitride. *Scientific Rep* (2016) 6:21202–8. doi:10.1038/srep21202

18. Gruenwald J. Proposal for a novel type of small scale aneutronic fusion reactor. *Plasma Phys Control Fusion* (2016) 59:025011. doi:10.1088/1361-6587/59/2/025011

19. Volosov VI. Aneutronic fusion on the base of asymmetrical centrifugal trap. *Nucl Fusion* (2006) 46:820–8. doi:10.1088/0029-5515/46/8/007

20. Giuffrida L, Belloni F, Margarone D, Petringa G, Milluzzo G, Scuderi V, et al. High-current stream of energetic α particles from laser-driven proton-boron fusion. *Phys Rev E* (2020) 101:013204. doi:10.1103/physreve.101.013204

21. Margarone D, Morace A, Bonvalet J, Abe Y, Kantarelou V, Raffestin D, et al. Generation of α-particle beams with a multi-kJ, peta-watt class laser system. *Front Phys* (2020) 8:561410. doi:10.3389/fphy.2020.00343

22. Schwoerer H, Pfotenhauer S, Jäckel O, Amthor KU, Liesfeld B, Ziegler W, et al. Laser-plasma acceleration of quasi-monoenergetic protons from microstructured targets. *Nature* (2006) 439:445–8. doi:10.1038/nature04492

23. Lübcke A, Andreev AA, Höhm S, Grunwald R, Ehrentraut L, Schnürer M. Prospects of target nanostructuring for laser proton acceleration. *Scientific Rep* (2017) 7:44030–8. doi:10.1038/srep44030

24. Zigler A, Palchan T, Bruner N, Schleifer E, Eisenmann S, Botton M, et al. 5.5-7.5A MeV proton generation by a moderate-intensity ultrashort-pulse laser interaction with H2O nanowire targets. *Phys Rev Lett* (2011) 106:134801. doi:10.1103/PhysRevLett.106.134801

25. Ruhl H, Korn G. A laser-driven mixed fuel nuclear fusion micro-reactor concept 2022.

26. Mehlhorn TA, Labun L, Hegelich BM, Margarone D, Gu MF, Batani D, et al. Path to increasing p-B11 reactivity via ps and ns lasers. *Laser Part Beams* (2022) 2022:e1. doi:10.1155/2022/2355629

27. Krainov VP. Theory of laser induced fusion in compound boron-hydrogen microdroplets. *Contrib Plasma Phys* (2005) 45:198–203. doi:10.1002/CTPP.200510021

28. Kaganovich D, Ting A, Moore CI, Zigler A, Burris HR, Ehrlich Y, et al. High efficiency guiding of terawatt subpicosecond laser pulses in a capillary discharge plasma channel. *Phys Rev E* (1999) 59:R4769–72. doi:10.1103/PhysRevE.59.R4769

29. Ehrlich Y, Cohen C, Zigler A, Krall J, Sprangle P, Esarey E. Guiding of high intensity laser pulses in straight and curved plasma channel experiments. *Phys Rev Lett* (1996) 77:4186–9. doi:10.1103/PhysRevLett.77.4186

30. Shalloo RJ, Dann SJD, Gruse JN, Underwood CID, Antoine AF, Arran C, et al. Automation and control of laser wakefield accelerators using Bayesian optimization. *Nat Commun* (2020) 11:6355–8. doi:10.1038/s41467-020-20245-6

31. Jalas S, Kirchen M, Messner P, Winkler P, Hübner L, Dirkwinkel J, et al. Bayesian optimization of a laser-plasma accelerator. *Phys Rev Lett* (2021) 126:104801. doi:10.1103/PHYSREVLETT.126.104801

32. Irshad F, Karsch S, Döpp A. Multi-objective and multi-fidelity Bayesian optimization of laser-plasma acceleration. *Phys Rev Res* (2023) 5:013063. doi:10.1103/physrevresearch.5.013063

33. Djordjević BZ, Kemp AJ, Kim J, Simpson RA, Wilks SC, Ma T, et al. Modeling laser-driven ion acceleration with deep learning. *Phys Plasmas* (2021) 28:43105. doi:10.1063/5.0045449

34. Döpp A, Eberle C, Howard S, Irshad F, Lin J, Streeter M. Data-driven science and machine learning methods in laser–plasma physics. *High Power Laser Sci Eng* (2023) 11:e55. doi:10.1017/hpl.2023.47

35. Schulz E, Speekenbrink M, Krause A. A tutorial on Gaussian process regression: modelling, exploring, and exploiting functions. *J Math Psychol* (2018) 85:1–16. doi:10.1016/J.JMP.2018.03.001

36. Krushelnick K, Ting A, Moore CI, Burris HR, Esarey E, Sprangle P, et al. Plasma Channel formation and guiding during high intensity short pulse laser plasma experiments. *Phys Rev Lett* (1997) 78:4047–50. doi:10.1103/PhysRevLett.78.4047

37. Arber TD, Bennett K, Brady CS, Lawrence-Douglas A, Ramsay MG, Sircombe NJ, et al. Contemporary particle-in-cell approach to laser-plasma modelling. *Plasma Phys Control Fusion* (2015) 57:113001. doi:10.1088/0741-3335/57/11/113001

38. Wriedt T. Mie theory: a review. *Springer Ser Opt Sci* (2012) 169:53–71. doi:10.1007/978-3-642-28738-1_2

39. Islam MR, Saalmann U, Rost JM. Kinetic energy of ions after Coulomb explosion of clusters induced by an intense laser pulse. *Phys Rev A* (2006) 73:041201. doi:10.1103/PHYSREVA.73.041201

40. Tentori A, Belloni F. Revisiting p-11B fusion cross section and reactivity, and their analytic approximations. *Nucl Fusion* (2023) 63:086001. doi:10.1088/1741-4326/ACDA4B

41. Jones DR, Schonlau M, Welch WJ. Efficient global optimization of expensive black-box functions. *J Glob Optimization* (1998) 13:455–92. doi:10.1023/A:1008306431147

42. Rasmussen CE, Williams CKI. Gaussian processes for machine learning. *Gaussian Process Machine Learn* (2005). doi:10.7551/MITPRESS/3206.001.0001

43. Frazier PI. A tutorial on bayesian optimization 2018.

44. Last I, Jortner J. Nuclear fusion induced by Coulomb explosion of heteronuclear clusters. *Phys Rev Lett* (2001) 87:033401–4. doi:10.1103/PHYSREVLETT.87.033401

45. Nishihara K, Amitani H, Murakami M, Bulanov S, Esirkepov T *High energy ions generated by laser driven Coulomb explosion of cluster*, 464 (2001).

46. Mora P. Plasma expansion into a vacuum. *Phys Rev Lett* (2003) 90:185002. doi:10.1103/PHYSREVLETT.90.185002

47. Margarone D, Velyhan A, Dostal J, Ullschmied J, Perin JP, Chatain D, et al. Proton acceleration driven by a nanosecond laser from a cryogenic thin solid-hydrogen ribbon. *Phys Rev X* (2016) 6:041030. doi:10.1103/physrevx.6.041030

48. Macchi A, Borghesi M, Passoni M. Ion acceleration by superintense laser-plasma interaction. *Rev Mod Phys* (2013) 85:751–93. doi:10.1103/revmodphys.85.751

49. Brenner CM, Robinson APL, Markey K, Scott RHH, Gray RJ, Rosinski M, et al. High energy conversion efficiency in laser-proton acceleration by controlling laser-energy deposition onto thin foil targets. *Appl Phys Lett* (2014) 104:11. doi:10.1063/1.4865812